Article:
Bradford, P., Dearling, A., Ehret, M. et al. (17 more authors) (2021) Measuring magnetic fields in laser-driven coils with dual-axis proton deflectometry. Plasma Physics and Controlled Fusion. 084008. ISSN 1361-6587

https://doi.org/10.1088/1361-6587/ac0bca

Plasma Physics and Controlled Fusion

Measuring magnetic fields in laser-driven coils with dual-axis proton deflectometry

OPEN ACCESS
IOP Publishing
Plasma Physics and Controlled Fusion
Plasma Phys. Control. Fusion **63** (2021) 084008 (13pp)
https://doi.org/10.1088/1361-6587/ac0bca

Measuring magnetic fields in laser-driven coils with dual-axis proton deflectometry

P Bradford[1,*], A Dearling[1], M Ehret[2,3], L Antonelli[1], N Booth[4], D C Carroll[4], R J Clarke[4], K Glize[9,10], R Heathcote[4], M Khan[1], J D Moody[5], S Pikuz[6,7], B B Pollock[5], M P Read[8], S Ryazantsev[6,7], C Spindloe[4], C P Ridgers[1], J J Santos[2], V T Tikhonchuk[2,11] and N C Woolsey[1,*]

[1] York Plasma Institute, Department of Physics, University of York, York, United Kingdom
[2] Centre Lasers Intenses et Applications, University of Bordeaux-CNRS-CEA, 33405 Talence, Bordeaux, France
[3] Institut für Kernphysik, Tech. Univ. Darmstadt, 64289 Darmstadt, Germany
[4] Central Laser Facility, Rutherford Appleton Laboratory, Chilton, Didcot, STFC, UKRI, Oxfordshire, United Kingdom
[5] Lawrence Livermore National Laboratory, Livermore, CA 94551, United States of America
[6] National Research Nuclear University MEPhI, Moscow 115409, Russia
[7] Joint Institute for High Temperatures, RAS, Moscow 125412, Russia
[8] First Light Fusion, Oxford Industrial Park, Kidlington OX5 1QU, United Kingdom
[9] Key Laboratory for Laser Plasmas (MOE), School of Physics and Astronomy, Shanghai Jiao Tong University, Shanghai 200240, People's Republic of China
[10] Collaborative Innovation Center for IFSA, Shanghai Jiao Tong University, Shanghai 200240, People's Republic of China
[11] ELI Beamlines, Institute of Physics, Czech Academy of Sciences, Za Radnicic 835, Dolní Břežany 25241, Czech Republic

E-mail: philip.bradford@york.ac.uk and nigel.woolsey@york.ac.uk

Received 8 April 2021, revised 27 May 2021
Accepted for publication 16 June 2021
Published 1 July 2021

Abstract

By driving hot electrons between two metal plates connected by a wire loop, high power lasers can generate multi-tesla, quasi-static magnetic fields in miniature coil targets. Many experiments involving laser-coil targets rely on proton deflectometry directed perpendicular to the coil axis to extract a measurement of the magnetic field. In this paper, we show that quantitative measurements using perpendicular probing are complicated by the presence of GV m^{-1} electric fields in the target that develop on sub-ns timescales. Probing parallel to the coil axis with fiducial grids is shown to reliably separate the electric and magnetic field measurements, giving current estimates of $I \approx 5$ kA in 1 mm- and 2 mm-diameter wire loops. An analytic model of proton deflection in electric and magnetic fields is used to benchmark results from the particle-in-cell code and help deconvolve the magnetic and electric field deflections. Results are used to motivate a new experimental scheme that combines a

* Authors to whom any correspondence should be addressed.

single-plate target with axial proton probing and direct current measurements. This scheme has several important advantages over the traditional target and diagnostic set-up, enabling the robust measurement of coil magnetic fields and plasma properties, as well as making it easier to validate different theoretical models at a range of laser intensities.

Keywords: magnetic, fields, laser, coils, proton deflectometry, proton radiography, plasma

(Some figures may appear in colour only in the online journal)

1. Introduction

Discharge currents are produced in all high power laser-solid interactions where a target is connected to ground. These currents are frequently disruptive, for instance when they emit bursts of radiofrequency EMP that couple to electronic equipment [1], although in other contexts they can be beneficial. Using specially-constructed helical targets, discharge pulses have been used to focus and energy-select proton beams accelerated off the back of metal foils [2–4]. In inertial confinement fusion (ICF) research, electron reflux and fuel preheat is reduced as a return current propagates along the target support and neutralises the target potential [5–7]. There is also a lot of interest in using the laser discharge current to magnetize a plasma. Multi-tesla, externally-applied magnetic fields can increase fusion yields in ICF [8–10], focus charged-particle beams [11, 12], or be used for applications in laboratory astrophysics [13–16].

To tailor these discharge currents to specific applications requires robust measurement and analysis techniques. Many experiments have used proton deflectometry to capture images of the electromagnetic fields around the coil, from which the spatial and temporal field profiles can be extracted. Proton beams are often directed perpendicular to the coil axis [13, 18, 19], producing a distinctive teardrop-shaped void that is circumscribed by a caustic. Figure 1 shows perpendicular radiographs taken from the experiment detailed in [17]. In the absence of electric fields, the width of the void at the top of the loop is proportional to the square root of the coil current and inversely proportional to the fourth root of the proton energy [19]. This means there is a strong link between the void diameter, d_v, the coil current and magnetic field. On the other hand, by probing perpendicularly across the coil, protons are deflected by strong fields around the wire surface and therefore carry little or no information about the field structure inside the loop itself [20]. There is moreover the issue of electric fields, which contribute towards d_v and substantially increase the errors associated with the magnetic field measurements.

Breaking the degeneracy of electric and magnetic field measurements in proton radiography is important for applications in magnetized high energy density physics and to help test predictive models of capacitor-coil operation [9, 21–27]. Here we present additional results and analysis from an experiment conducted on the Vulcan laser and previously reported in [17]. The dual-axis experimental scheme can be seen in figure 2. Capacitor coil targets were irradiated by three long-pulse laser beams overlapped on their rear plates for a combined energy of $E_L = 550$ J and a focal intensity of $\sim 5 \times 10^{15}$ Wcm^{-2}. Each drive beam consisted of a 1 ns-duration square pulse with ~100 ps rise time and wavelength $\lambda_L = 1.053$ μm. Proton beams were accelerated off 40 μm-thick Au foils via the target normal sheath acceleration (TNSA) mechanism [28], eventually passing across a capacitor-coil target and being deposited on stacks of radiochromic film (RCF). Using proton deflectometry along two orthogonal axes, the evolution of electric and magnetic fields in capacitor-coil targets can be reliably inferred. Electromagnetic field profiles were found to be reproducible over tens of laser shots, with a likely peak magnetic field of $B_0 \approx 5$ T achieved at the centre of the 1 mm-diameter coils[12]. Lessons learned from the dual-axis probing experiment are used to motivate a single-plate experimental scheme that combines proton deflectometry along the loop axis with a direct voltage or current diagnostic. Similar to other experiments involving single-plate coils [20, 29, 30], this simplified approach makes it easier to diagnose plasma properties and particles ejected from the laser focal spot. It also provides a reliable supporting diagnostic of the return current, which can be studied for a wide range of laser parameters.

The techniques outlined in this paper are testament to the lasting influence of the late Prof. David Neely on diagnostics of magnetic and electric fields in experiments with high power lasers. David's work spanned the entire field of high power laser science, from laser technology to plasma physics, facility operation and diagnostic development [31, 32]. He was interested in what could be learned from radiation and charged particles emitted from the laser focal spot [33–35] and reciprocally how laser and target properties could be manipulated to produce new radiation sources [36–38]. He also played a pivotal role in the development of proton deflectometry with RCF imaging [39], using them to measure electromagnetic fields in laser-plasmas [40, 41] and discharge pulses propagating along conducting surfaces [42]. David possessed an uncommonly clear intellect that helped produce novel measuring instruments [43–45] and his ideas have been influential in the fields of ion acceleration [46–48], electron dynamics and sheath formation [49, 50], charged particle radiography and high-frequency radiation sources [1, 37, 51–53]. Many of these advances are directly applicable to the physics of

[12] We would like to take this opportunity to correct the magnification of the proton deflectometry diagnostic reported in [17]. The magnification was 7 - not 10 - which means the inferred currents and charges are slightly larger than previously observed. In addition, figure 10 in [17] has an erroneous magnetic field profile. Our conclusions about grid deflection close to the wire surface are not significantly changed, however.

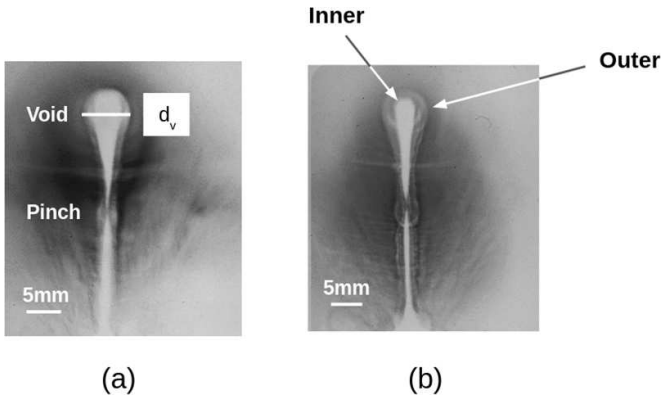

Figure 1. Proton radiographs of capacitor-coil targets taken during an experiment on the Vulcan laser, where the proton beam is oriented perpendicular to the coil axis and anti-parallel to the current at the top of the loop [17]. Both images were made using $\epsilon_p = 7.3$ MeV protons passing across 2 mm-diameter coil targets shortly after the end of the ns-duration laser drive. Darker colours represent a higher proton signal. (a) Radiograph with void and pinch features labelled, indicating the presence of a strong magnetic field. Adapted from [17]. CC BY 4.0. (b) Radiograph with a compound void structure consisting of an inner lobe that is devoid of protons and an outer halo that is partially filled.

laser-driven magnetic fields and continue to inform our work on capacitor-coil targets.

This paper is divided into several sections. Section 2 presents an analytic model of proton deflection in static EM fields around a straight wire that can be used to extract a rough estimate of the loop current and magnetic field. In section 3, simulation results from perpendicular probing of the coil are presented. They suggest that strong electromagnetic fields are present in the target that require alternative approaches to produce a reliable quantitative field measurement. In section 4, simulations of proton deflectometry parallel to the loop axis show that the magnetic field can be uniquely determined from proton beam rotation inside the coil. Comparison with RCF data suggests that no measurable magnetic fields were produced in the coil during our experiment, giving likely upper limits on the wire current of a few kA. In section 5, the analytic model is used to infer the scaling of proton caustic radius with proton energy, providing an alternative means of separating electric and magnetic fields in proton deflectometry. Finally, in section 6, the Vulcan experimental results are used to motivate a new experimental scheme that could significantly improve future magnetic field measurements and models of optical magnetic field sources. Data to support the findings in this study is openly available at [54].

2. Analytic model of caustic formation for proton probing perpendicular to the coil axis

In this section, we introduce an analytic formula for the width of the teardrop-shaped proton void that is observed in RCF images of capacitor coil targets (see figure 1). In [19], Gao *et al* derive an expression for the caustic radius when a monoenergetic proton beam passes through a static capacitor coil magnetic field. The magnetic field of an infinite straight wire, distributed over a short[13] distance Δz, is used to approximate the magnetic field at the top of a wire coil. Here, we extend Gao's method to account for a monoenergetic proton beam passing through electric and magnetic fields corresponding to a charged, current-carrying straight wire. A diagram of the coordinate system can be seen in figure 3. The charge and current distributions are considered static and uniformly-distributed over the wire, with electromagnetic fields confined to a region of spatial extent Δz. The beam is oriented anti-parallel to the wire current such that each proton is deflected radially away from the wire surface by the Lorentz force. For protons of fixed energy ε_p, system magnification M and target-detector distance D, a circular caustic will form in the image plane with radius:

$$r_v = 2\sqrt{MD\Delta z(\mu_E + \mu_B)} \tag{1}$$

where $\mu_B = \frac{e\mu_0 I}{2\pi\sqrt{2m_p\epsilon_p}}$, $\mu_E = \frac{e\lambda}{4\pi\epsilon_0\epsilon_p}$, I is the wire current, λ the linear charge density, m_p the mass of a proton and μ_0 and ε_0 the permeability and permittivity of free space. A full derivation of equation (1) is provided in the appendix. Equation (1) implies that $r_v \propto I^{\frac{1}{2}}$ and $r_v \propto \epsilon_p^{-\frac{1}{4}}$ for a proton beam passing through the magnetic field at the top a wire loop, whilst $r_v \propto \lambda^{\frac{1}{2}}$ and $r_v \propto \epsilon_p^{-\frac{1}{2}}$ in the electric field around a charged wire. Neglecting the electric field term μ_E in equation (1), an estimate of the on-axis coil magnetic field can be extracted given a measurement of the caustic width d_v and an assumed value of Δz:

$$d_v = 4\left(\frac{e\mu_0 I\Delta z MD}{2\pi}\right)^{\frac{1}{2}}\left(\frac{1}{2m_p\epsilon_p}\right)^{\frac{1}{4}}. \tag{2}$$

Figure 4 shows how d_v varies with proton energy and coil magnetic field. The magnetic field at the coil centre is estimated via $B_0 = \mu_0 I/2R$ and the white contour lines represent the range of void widths observed on the Vulcan experiment in [17]. Since the TNSA protons generated during the experiment had energy $\epsilon_p < 15$ MeV, the figure suggests that wire currents and on-axis magnetic fields were below ~25 kA and ~30 T respectively. If the μ_B term is neglected in equation (1) and the μ_E term retained, the impact of electric fields on proton radiography of the coil can be estimated. We find that for a linear charge density of $\lambda = 5$ nC mm^{-1}, a mm-sized loop can produce multi-mm diameter caustics that are comparable to those from multi-tesla magnetic fields.

3. Deflectometry perpendicular to loop axis

Particle-in-cell (PIC) simulations allow us to model proton deflections in electric and magnetic fields around a wire of arbitrary shape. Details of our synthetic radiography

[13] short with respect to the source-target and target-detector distances.

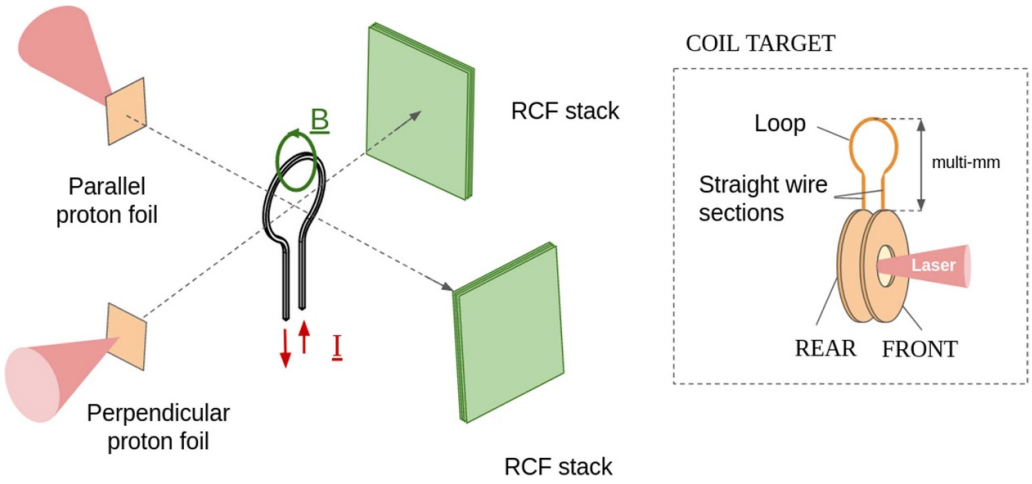

Figure 2. Schematic representation of the dual-axis experiment. Two Cu foils were placed orthogonally and irradiated with ps-duration lasers, firing TNSA proton beams across the capacitor-coil target (plates not shown) and onto the RCF detectors. Cu grids were interposed between the proton foil and the capacitor-coil on several shots in order to imprint a mesh fiducial into the proton images. The loop current I and corresponding magnetic field B are indicated with arrows in red and green, while the dashed lines represent the two orthogonal axes of the proton beams. Spatial dimensions are grossly exaggerated in this image. The proton foil-target distance was 12 mm and the target-RCF distance was 70 mm for a coil magnification of ≈7—this is corrected from a magnification of 10 in [17]. Inset on the right-hand side is a diagram of the coil target. Underneath the wire loop are two straight wire sections that connect the front and rear plates together. The rear plate was supported by an insulating rod that separated the target from the ground.

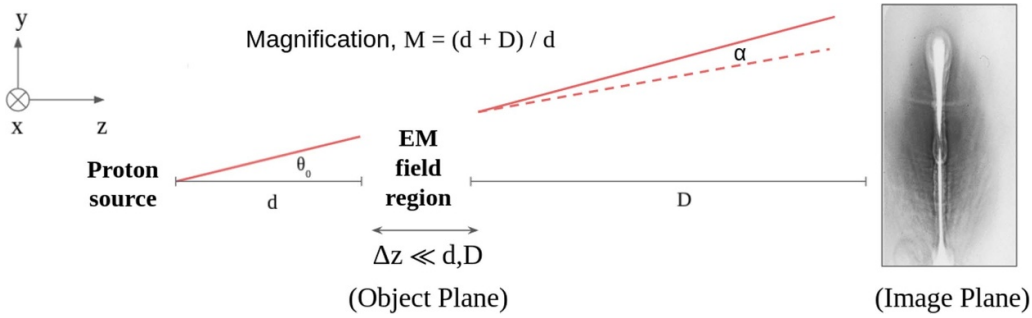

Figure 3. Diagram of our coordinate system. A straight wire of static and uniform current, I, is oriented along the z-axis. The corresponding magnetic field is constant at a fixed radius from the wire centre with a value B_r. The wire is also uniformly charged with radial electric field E_r at a fixed radius from the wire.

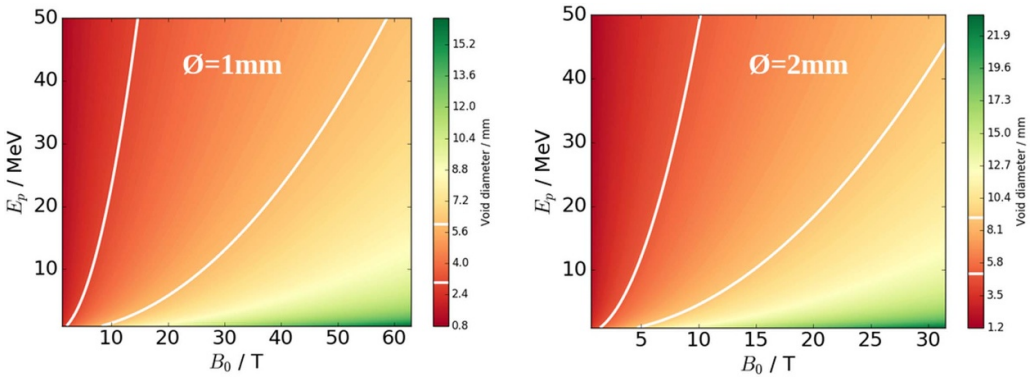

Figure 4. Filled contour plots of proton void diameter for proton deflection around 1- and 2 mm-diameter capacitor coils. The void diameter is plotted for different proton energies and magnetic fields. The void diameter is calculated using the analytic method from [19] and geometrical parameters are taken from the Vulcan experimental set-up. The white contour lines demarcate the range of void sizes observed on our experiment. For example, most shots with 1 mm loops produced voids between 3 and 6 mm across.

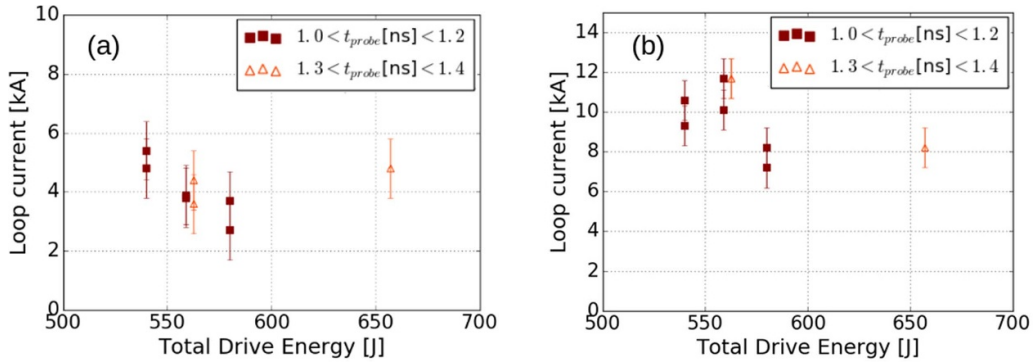

Figure 5. Variation in loop current with total applied laser energy for 1 mm-diameter capacitor coil targets. The loop current is inferred from B-field only simulations using measurements of (a) inner void diameter (b) outer halo diameter. Corresponding target probe times are shown in the legends.

technique can be found in [17]. Synthetic radiographs were benchmarked against the analytic model from section 2. The results presented in this section were run with proton beams oriented perpendicular to the coil axis passing through static magnetic fields.

Experimental radiographs captured later than $t \sim 0.5$ ns into the laser drive feature proton voids with a two-layer structure, as illustrated in figure 1(b). The inner void contains no proton signal, whereas the outer halo is structured and partially filled. Since our magnetic field simulations only produce a single void, one can choose whether to fit the void diameter to the inner or outer caustic. Figure 5 shows how the capacitor coil current varies with applied laser energy for targets with 1 mm-diameter loops, 1–1.4 ns after the beginning of the laser drive. These current measurements are inferred from the inner void diameter (figure 5(a)) and outer halo diameter (figure 5(b)). They do not change significantly for laser energies between 540 J and 660 J.

The temporal evolution of the capacitor coil current is plotted in figure 6 for 1 mm and 2 mm-diameter loops. Values are inferred from a series of shots taken at different probe times with on-target laser energies between 540 J and 660 J. Since the loop current appears to be stable with laser energy in this range, the data in figure 6 has not been normalised. Error bars are slightly larger for the data points at $t_{\mathrm{probe}} < 0.5$ ns because the proton beam was oriented at an oblique angle to the loop that has been estimated from RCF images. Both 1 mm and 2 mm loop targets exhibit similar behaviour. Figure 6 suggests the magnetic field rises to a maximum a few hundred picoseconds after the beginning of the laser drive, decays to under half its maximum value in the same time and then remains approximately constant for at least a further nanosecond. This behaviour is not consistent with the dynamics of the laser ablation current or consideration of the target in terms of a lumped-element circuit. It is therefore important to compare the qualitative features of the radiographs early and late in the laser drive to see if electric fields should be included in our simulations as well.

Figure 7 shows RCF data taken at two extremes of the laser drive. In figure 7(a), a single-plate target is captured $t \approx 300$ ps after the beginning of the laser pulse. The single-plate target is identical to our standard two-plate

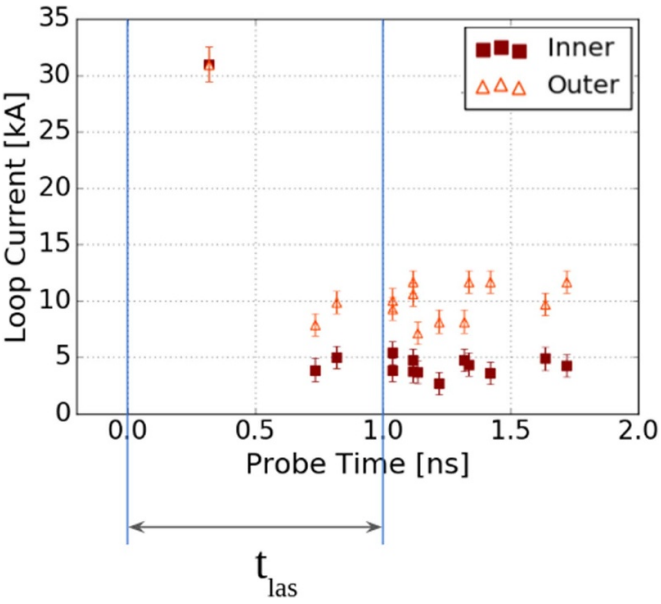

Figure 6. Temporal evolution of B-field for 1 mm-diameter capacitor coil targets. The laser arrives at time $t_{\mathrm{probe}} = 0$ ns. Red squares indicate inner void measurements, while orange triangles represent measurements of the outer halo.

design (inset to figure 2) except that the front plate has been removed. Matching proton deflections around the wire to synthetic radiographs with static magnetic fields, the inferred current for the vertical wire sections underneath the loop ($I = 200$ kA, figure 7(a.i)) is much higher than the current needed to reproduce the void at the apex of the loop ($I = 40$ kA, figure 7(a.ii)). This is because protons passing underneath the loop are moving almost parallel to the magnetic field lines, so the magnetic component of the Lorentz force is relatively small. The absence of a strong pinch to complement the void is further evidence that a positive electric field is present (since the laser is still charging the target, it is unreasonable to suppose the deflections can be explained by a current inhomogeneity). These observations, which are common to radiographs of single and two-plate targets probed a few hundred ps after the laser drive, suggest that GV m^{-1} electric

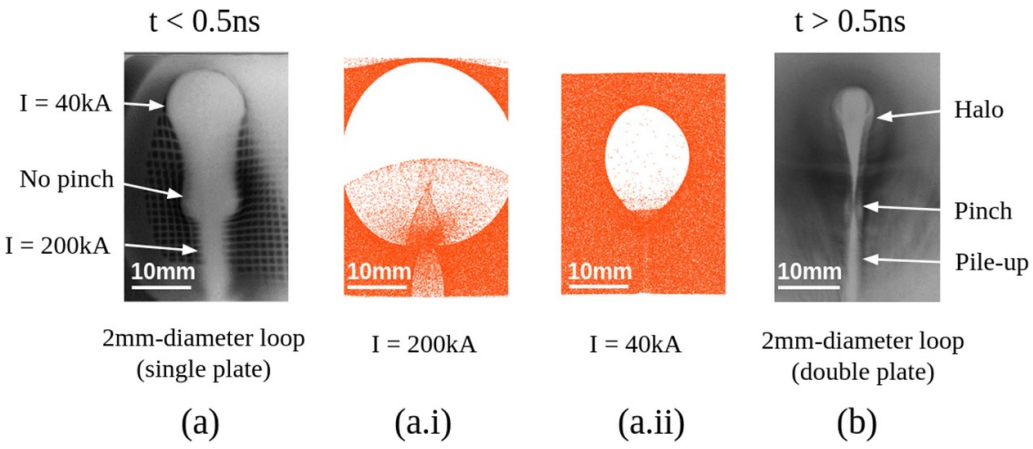

Figure 7. (a) Experimental radiograph corresponding to protons with energy $\epsilon_p = 10.6$ MeV, probing the target at $t \approx 0.3$ ns after the beginning of the laser drive. Current estimates based on magnetic field simulations at the top of the loop ($I = 40$ kA) and the vertical wires ($I = 200$ kA) are inconsistent. (a.i) Synthetic radiograph generated using $\epsilon_p = 10.6$ MeV protons for a 2 mm-diameter loop carrying a 200 kA static current in the experimental geometry. (a.ii) Synthetic radiograph generated using $\epsilon_p = 10.6$ MeV protons for a 2 mm-diameter loop carrying a 40 kA static current in the experimental geometry. (b) Experimental radiograph corresponding to protons with energy $\epsilon_p = 7.3$ MeV, probing the target at $t \approx 1.2$ ns after the beginning of the laser drive. Adapted from [17]. CC BY 4.0.

fields at the wire surface have a dominant impact on proton deflections around the wire.

Figure 7(b) is representative of radiographs taken towards the end of the laser drive. An inverse teardrop-shaped caustic is evidence of a significant magnetic field. We find that the void and pinch structure cannot be reproduced without a magnetic field, using realistic simulations of electric charge placed in and around the loop. Furthermore, experiments at the LULI facility have demonstrated that when the coil is driven in the opposite sense, the proton void flips vertically to form a teardrop [18]. While the magnetic field appears to dominate at these late times, a pile-up of protons around the shadow of the wire provides evidence for plasma sheath electric fields. An intricate bubble-like structure (see figure 1(b)) and separation of the caustic from the shadow of the wire suggests it is not caused by scattering off the target. Simulations show that an inner void surrounded by a secondary, partially-filled halo with outer caustic can be formed if (a) an annulus of negative charge is placed around a positively charged wire, with a uniform current density flowing in the negatively-charged region (b) or, alternatively, a positive radial electric field emanating from the wire is abruptly cut off at a short distance from the surface where a current is flowing. Both of these scenarios are broadly consistent with a plasma sheath field present at the wire surface. Around the loop, the proton pile-up forms an outer halo that is clearly visible in figures 1(b) and 7(b). This compound void structure is not caused by background signal from the high energy protons depositing energy in early layers of RCF because the proton beam cuts off at 15 MeV and the outer halo was observed in radiographs corresponding to protons of this energy. It is therefore possible that the inner void, which contains no proton signal, is caused by magnetic fields, whereas the more diffuse outer halo may be a product of extended electric fields in a plasma surrounding the solid wire. The picture is similar to those proposed by Peebles *et al* [20] and Manuel *et al* [6], where the loop current flows through a plasma surrounding the wire along a low-impedance pathway. Plasma formation on the wire has been observed through shadowgraphic imaging of an experimental coil [21] as well as in multi-physics simulations of capacitor-coil operation [29]. Depending on the amplitude and extent of the charge distribution, sheath fields can inflate or reduce the void diameter slightly compared with current-only simulations. The impact of the plasma is therefore to increase the vertical error in figures 5 and 6 by several kA.

Evidence for electric fields throughout the laser drive and the complexity of the corresponding current and charge geometry suggests that additional data is needed to extract a reliable measurement of the coil magnetic field. In the next sections, we describe how axial deflectometry and proton energy scalings can be used to help break the degeneracy of the electromagnetic field measurements.

4. Deflectometry parallel to the loop axis

When a proton beam passes axially through a current loop, the loop magnetic field causes the beam to rotate through a fixed angle. If a high-Z grid is used to imprint a mesh structure in the beam spatial profile, the rotation of the grid shadow can be measured and an estimate of the magnetic field extracted [17, 20, 24]. Crucially, grid rotation is independent of radial electric fields and beam divergence angle. Though axial probing was conducted on our Vulcan experiment, the magnetic fields were too low to produce a measurable rotation. Simulations with thin current-carrying wires in the experimental geometry show that the grid rotation angle increases linearly with current, producing a rotation of $\sim 2^\circ$ at $I = 20$ kA. Since the spatial resolution of proton deflectometry is generally very high, the sensitivity of an axial probing measurement will depend primarily on the strength and distribution of electric fields around the target. Evidence of 0.5 mm-scale distortions in the grid profile caused by GV m^{-1} non-uniform

electric fields suggests it would be difficult to resolve a rotation caused by currents below $I \approx 20$ kA. This upper limit is consistent with current estimates based on the void diameter in perpendicular radiographs. The sensitivity of proton deflectometry is higher when conducted perpendicular rather than parallel to the loop axis because the protons pass through a more extended magnetic field. Equation (2) indicates that the proton void diameter approaches the apparent wire diameter for kA-level currents and ∼5 MeV proton energies, giving a sensitivity of $\geqslant$1kA in the perpendicular orientation.

Probing simultaneously along both axes of the coil allows us to check our electromagnetic field measurements for consistency. Figure 8 shows perpendicular and axial radiographs for a single-plate target probed early in the interaction, $t_{\text{probe}} = 0.3$ ns after the beginning of the laser drive. The perpendicular radiograph in figure 8(a) features a substantial void at the top of the 2 mm-diameter loop and strong proton deflections all along the length of the straight wire sections. Since magnetic field deflections are small around the straight wire sections for currents below ∼50 kA, electric field simulations were run to match deflections around these wires before magnetic fields were added to enlarge the void at the top of the loop. The optimised results can be seen in figure 8(b), for a wire current of 15 kA and wire charge of 60 nC, with the charge spread uniformly across the full length of the wire loop for a linear charge density of $\lambda = 6.7$ nC mm^{-1} and an electric field at the wire surface of $\sim 10^9$ Vm^{-1}. This positive wire charge can be seen as a portion of the total positive charge left in the target by escaping hot electrons. It represents a small fraction of the total charge transported between the capacitor plates, since a 5 kA current flowing for 1 ns will transport 5000 nC of charge. Figure 6 suggests that a quasi-static current is established with a delay of ∼ 0.5 ns. During this initial time interval, a charge has already accumulated on the target but it is not yet transferred to the ground; electrical charging of the coil can therefore be considered part of the transient discharge process. Turning now to the axial radiograph in figure 8(c), a faint caustic can be distinguished around the outside of the wire which has been demarcated by dashed lines set ∼1.5 mm from the wire centre. A wire current of 40 kA is required to produce an apparent wire thickness of 1 mm in the axial orientation. Since the absence of grid rotation places an upper limit on the current of $I \approx 20$ kA, we have ignored the current in axial simulations. A wire linear charge density of 3.3 nC mm^{-1} gives a caustic width of 3 mm, which matches the caustic on the outside of the wire (see figure 8(d)). This is approximately half the charge density and electric field inferred from figure 8(a).

The discrepancy between the EM fields inferred from axial and perpendicular deflectometry suggests that the assumption of thin, static and uniform charge and current densities is too simplistic. Extended charge profiles are needed to reproduce the outer halo features in late-time perpendicular radiographs and free charges in the coil may affect the spatial distribution of the magnetic field as well.

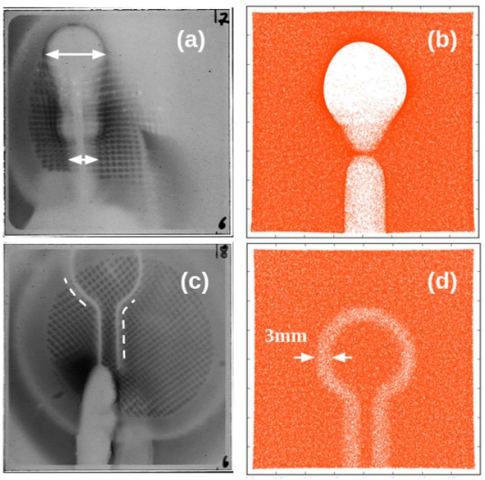

Figure 8. Simultaneous proton probing of a 2 mm-diameter single-plate capacitor coil target (a) perpendicular radiograph with $t_{\text{probe}} = 0.3$ ns and $\epsilon_{\text{p}} = 7.3$ MeV protons. (b) Combined E- and B-field PIC simulation with wire current $I = 15$ kA and wire charge $Q = +60$ nC. (c) Axial radiograph with $t_{\text{probe}} = 0.3$ ns and $\epsilon_{\text{p}} = 7.3$ MeV protons. (d) EPOCH E-field only simulation with $Q = +30$ nC wire charge.

5. Scaling of radiographic features with proton energy

When a proton passes through an electric or magnetic field, the amount of deflection it experiences will depend on its kinetic energy. In section 2, the proton void diameter was shown to vary as $\epsilon_{\text{p}}^{-\frac{1}{4}}$ in a magnetic field and $\epsilon_{\text{p}}^{-\frac{1}{2}}$ in an electric field. In an electromagnetic field, the void diameter will vary as a combination of these two factors depending on the relative strength of the electric and magnetic fields. These proton energy scalings can be used to try to discriminate between features in the radiographs that derive from a dominant electric field and those from a dominant magnetic field.

Referring to the experimental radiographs (see figure 9), the energy dependence of the inner void and outer halo were tested separately to see if there was a difference between the two. The void diameter was measured on RCF layer 4 ($\epsilon_{\text{p}} = 5.6$ MeV) and RCF layer 11 ($\epsilon_{\text{p}} = 14.6$ MeV), then the ratio of these values were compared to the expected energy scalings. The boundary of each void was identified by taking the average of five horizontal lineouts of the proton signal and recording local minima. Results suggest the inner void matches the magnetic field scaling well on those shots where an inner void can be reliably distinguished ($t_{\text{probe}} > 0.5$ ns). Though the outer halo varies more strongly than the magnetic field scaling on some shots, it is always closer to $\epsilon_{\text{p}}^{-\frac{1}{4}}$ than $\epsilon_{\text{p}}^{-\frac{1}{2}}$. In figure 9, a scatter plot shows how proton deflections scale with proton energy for a typical laser shot with $t_{\text{probe}} > 1.1$ ns. Both the inner void (blue dots) and outer halo (orange dots) decrease steadily as proton energy increases over a range of ∼10 MeV. Straight line fits to the experimental data illustrate how the outer halo diameter scales more strongly with ϵ_{p} than

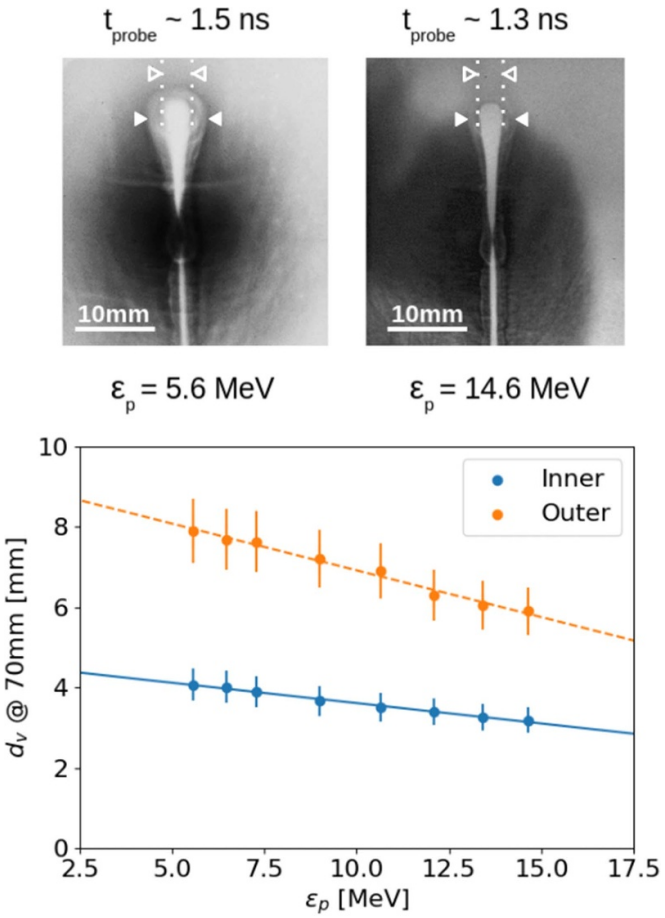

Figure 9. Experimental data corresponding to a single laser shot. Two experimental radiographs of the same capacitor coil target are shown at the top of the image, probed by $\epsilon_p = 5.6$ MeV and $\epsilon_p = 14.6$ MeV protons. Filled and un-filled arrows mark the dimensions of the outer halo and inner void diameter respectively. Underneath, void diameter d_v is plotted against proton energy for several layers of RCF that were irradiated on the same shot. The void diameter measured on each layer of RCF has been re-scaled to the same position, $D = 70$ mm from the centre of the capacitor coil loop. Vertical errors are dominated by uncertainty in the position of the RCF stack relative to the proton foil. Horizontal errors of order 0.1 MeV are too small to be shown. Solid and dashed straight lines represent least squares fits to the inner and outer void diameter data respectively.

the inner void. The void diameter of the single-plate target shown in figure 8(a), which appears to show good qualitative evidence for electric fields, is almost constant with proton energy.

Rapid changes in capacitor coil fields could be responsible for a deviation from the expected proton energy scaling. This is particularly important early in the interaction, when the current could be rising as fast as 100 kA ns^{-1} alongside GV m^{-1} electric fields. At later times ($t_{\text{probe}} >$ 0.7 ns) the coil current and sheath electric fields appear to be roughly constant, so correcting for dynamic fields is less important. Using higher energy protons may help improve the agreement between experimental results and the expected ϵ_p-scalings.

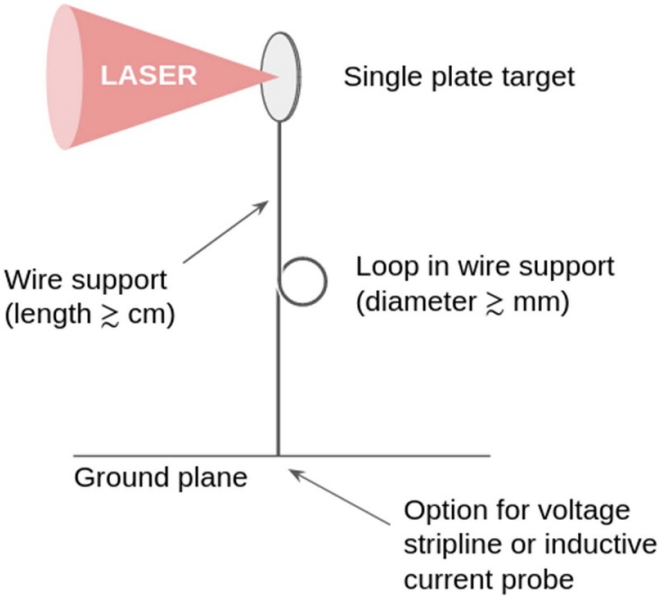

Figure 10. Experimental platform for measurement of fast currents and multi-tesla magnetic fields.

6. Discussion and implications for future experiments

The experiment described in this paper and [17, 54] suggests that single-plate targets can produce strong electromagnetic fields and that axial proton radiography is essential to extract quantitative estimates of the electric and magnetic field. We can use these results to motivate a new experimental platform for measuring strong electromagnetic fields produced by the laser-induced charging of solid targets. The three main ingredients are: (a) a single-plate geometry with connected wire stalk (b) a mm-sized loop in the stalk for axial deflectometric probing (c) a direct current [55] or voltage [56, 57] diagnostic connected to the base of the stalk. Conducting or electro-optic [58] probes can be used to support the deflectometry diagnostic in the far-field and near-field respectively. A diagram of the proposed experiment can be seen in figure 10.

Single-plate targets are easier to model because the impact of photoionisation and plasma shorting effects on a second plate can be neglected. An open geometry also has important practical advantages over a two-plate scheme: First, it affords easy access for multiple short and long-pulse drive beams, opening up the possibility of magnetic field measurements taken over a broad range of laser intensities and plasma scale lengths. Second, it is easier to make measurements of plasma conditions and ejected particles that are crucial when trying to compare different models of laser-induced target charging. A very approximate upper bound on the ablation current I_0 from a laser target is given by:

$$I_0 = e n_h v_h A_{spot} \tag{3}$$

where n_h is the hot electron density, $v_h = \sqrt{k_B T_h / m_e}$ is the average 1D hot electron velocity at an electron temperature T_h

and A_{spot} is the area of the laser focal spot. While the hot electron velocity can be related to the plasma temperature and A_{spot} is known, the density of escaped electrons is sensitive to the experimental set-up via the target potential and proximity to ground. Although the target electrostatic voltage [59], plasma sheath fields and transverse motion of the laser-plasma column [21, 27] will limit the current to much lower values than that provided by equation (3), the ablation current remains intimately linked to plasma density and temperature in the laser focal spot.

The target support can be fashioned into a loop for use in various applications [2–4, 11] or as part of an axial deflectometry diagnostic [17, 20, 24]. Particle tracing simulations suggest that proton probing parallel to the loop axis with grid fiducials can reliably separate electric and magnetic field measurements. Loop diameter and grid magnification should therefore be carefully chosen so that the grid is visible inside the loop and an estimate of the magnetic field profile can be extracted. If the loop is positioned in the middle of the stalk, at a distance of several centimetres from the laser-plasma, the chance of hot electrons reaching the loop and perturbing radiographic measurements is significantly reduced compared with the standard two-plate capacitor-coil geometry.

Direct current or voltage probes attached to the base of the target holder can provide a robust independent measure of the return current profile and accumulated target charge. This is particularly advantageous if the wire current is expected to be below $I \approx 20$ kA, when grid rotation may be undetectable in axial proton images. Voltage stripline diagnostics have been demonstrated at both high [56] and medium [57, 60] laser intensity. Since the stripline connection is far away from the interaction point, shorting of electrical contacts due to x-ray flashover (see [61]) should be reduced. Another advantage of the voltage stripline scheme is that it is compatible with high rep-rate laser systems, which are becoming increasingly common. Alternatively, a Rogowski coil or similar inductive current probe [55, 62] can be used to measure the current passing through the stalk. For EMP studies, B-dot probe signals can be compared with target charge measurements and an antenna emission model [63].

7. Conclusion

In this paper, we have shown that electric fields are present in and around laser-driven coils at all stages of the laser interaction and that they affect the magnetic field measurements inferred from proton radiographs oriented perpendicular to the coil axis. Magnetic field measurements based on rotation of the proton beam parallel to the coil axis are particularly important because the rotation is independent of radial electric fields. When probing the target towards the end of the laser drive, a compound void structure provides evidence for an extended plasma with sheath electric fields oriented away from the wire surface. Early in the laser drive, simultaneous dual-axis probing reveals non-uniform GV m^{-1} electric fields emanating from the wire. The assumption of a thin, uniform charge and current density is too simplistic to reproduce all of the details of the experimental radiographs. PIC simulations with fine-mesh fiducials and extended electric fields are therefore needed to better constrain errors in deflectometry measurements. Any departure from an idealised current geometry will have important implications for B-dot and Faraday rotation measurements.

Reproducible quasi-static magnetic fields are observed at the end of the ns-duration laser drive, showing good agreement with simulations for wire currents of $I \approx 5$ kA. Magnetic fields inside the coil are too low to be detected in the axial proton radiographs, placing an upper limit on the wire current of ≈20 kA. Axial deflectometry may be a more useful diagnostic of larger currents or more extended magnetic fields, for instance in cylindrical coil or Helmholtz targets [9, 23, 27]. The scaling of the proton void with proton energy agrees well with an analytic model of proton deflection around a wire when probing towards the end of the laser drive. Relatively low proton energies combined with fast-rising currents and electric fields may explain a deviation from theory earlier in time.

Our dual-axis results have motivated an alternative experimental platform suitable for magnetic field measurements across a wide intensity range. The combination of axial proton deflectometry and a direct current probe could significantly improve the characterisation of return currents in the target stalk, while a single-plate geometry makes it easier to diagnose plasma properties and test models of target charging.

Data availability statement

The data that support the findings of this study are openly available at the following URL/DOI: http://dx. doi.org/10.15 124/79ca0a38-dddb-480c-9edf-d8f52496dfad.

Acknowledgments

The authors would like to acknowledge valuable discussions with J Davies, J Peebles and C Danson. They would also like to thank staff at the Central Laser Facility for their dedication to our experiment. This paper was supported by the LLNL Academic Partnership in ICF, EPSRC grants EP/L01663X/1 and EP/L000644/1 and the Czech Republic MSMT targeted support of Large Infrastructures, ELI Beamlines Project LQ1606 of the National Programme of Sustainability II. We have also received funding from the EUROfusion Consortium via Euratom research and training programme 2014-2018 under grant agreement No. 633053. The views and opinions expressed herein do not necessarily reflect those of the European Commission. The contribution of JIHT RAS team was completed within the framework of the Russian Ministry state assignment for Science and Higher Education (topic #01201357846).

Appendix

In this section we will derive an equation for proton deflection in the fields around a charged, current-carrying wire. This is an extension of the work presented in [19], where Kugland's mapping relation [64] between a point proton source and proton radiograph was applied to the case of a capacitor-coil loop in the absence of electric fields. Figure 3 shows the coordinate system and important parameters in the derivation. The wire is straight and located in the EM field region, aligned coaxially with the proton beam. The proton source is separated from the EM field region by a distance d, which in turn is separated from a detector by a distance D. A proton ray passing through a point will be defined by a pair of Cartesian coordinates (x, y) in the object plane and a point (x_i, y_i) in the image plane. For small angles of incidence θ_0 and deflection α from the object plane, we can assume that $\tan(\theta_0) \approx \theta_0$ and $\tan(\alpha) \approx \alpha$. This leads to a simple mapping equation between x and x_i [64]:

$$x_i = Mx + D\alpha_x$$
$$y_i = My + D\alpha_y$$

where M is the magnification of the imaging system ($M = \frac{d+D}{d}$). The deflection angles α_x and α_y are related to the proton velocity $\underline{v} = (v_x, v_y, v_z)$ by:

$$\alpha_x = \frac{v_x}{v_z}$$
$$\alpha_y = \frac{v_y}{v_z}.$$

The Lorentz force on a proton with velocity $\underline{v}$ is:

$$\ddot{\underline{x}} = \frac{e}{m_p}(\underline{E} + \underline{v} \times \underline{B})$$

Taking the x and y components of the cross product gives:

$$\ddot{x} = \frac{eE_x}{m_p} - \frac{e}{m_p} v_z B_y$$
$$\ddot{y} = \frac{eE_y}{m_p} + \frac{e}{m_p} v_z B_x.$$

Then integrating these equations yields the velocity components v_x and v_y:

$$v_x = \frac{e}{m_p} \int (E_x - v_z B_y) dt$$
$$v_y = \frac{e}{m_p} \int (E_y + v_z B_x) dt.$$

Splitting terms in E and B and changing the limits of integration from time to distance ($dt = dz\frac{dt}{dz} = \frac{1}{v_z} dz$) yields for v_x:

$$v_x = \frac{e}{m_p v_z} \int E_x dz - \frac{e}{m_p} \int B_y dz.$$

From which the deflection angles are obtained:

$$\alpha_x = \frac{e}{m_p v_z^2} \int E_x dz - \frac{e}{m_p v_z} \int B_y dz$$
$$\alpha_y = \frac{e}{m_p v_z^2} \int E_y dz + \frac{e}{m_p v_z} \int B_x dz.$$

These equations connect the proton deflection angles to the electric and magnetic field provided the angles of incidence and deflection are sufficiently small. Rewriting in terms of the non-relativistic proton kinetic energy ($\epsilon_\mathrm{p} = \frac{1}{2} m_\mathrm{p} v^2$) yields two equations that are valid for the protons generated in our experiment, with energies $\epsilon_\mathrm{p} \lesssim 15$ MeV:

$$\alpha_x = \frac{e}{2\,\epsilon_\mathrm{p}} \int E_x dz - \frac{e}{\sqrt{2 m_\mathrm{p} \epsilon_\mathrm{p}}} \int B_y dz$$
$$\alpha_y = \frac{e}{2\,\epsilon_\mathrm{p}} \int E_y dz + \frac{e}{\sqrt{2 m_\mathrm{p} \epsilon_\mathrm{p}}} \int B_x dz.$$

Since the case of protons deflected by the magnetic field around an infinite straight wire carrying a uniform current has been dealt with in [19], we can restrict ourselves to electric field deflections without loss of generality. Consider an electric field emanating from an infinitely long, uniformly charged wire. This infinite wire is oriented along the z-axis, with a radially-symmetric E-field given by:

$$E(r) = \frac{\lambda}{2\pi\epsilon_0 r} \qquad (r \geqslant R_0)$$

Here, λ is the wire charge per unit length, R_0 is the wire radius and the radial coordinate is $r = \sqrt{x^2 + y^2}$. The electric field is oriented radially away from the wire surface everywhere in space and therefore:

$$E_x = E(r)\cos(\theta) = E\frac{x}{r}$$
$$E_y = E(r)\sin(\theta) = E\frac{y}{r}$$

where θ is the standard polar angular coordinate (measured from the positive x-axis in the xy-plane). Substituting for $E(r)$ gives:

$$E_x = \frac{\lambda x}{2\pi\epsilon_0 r^2} \qquad (r \geqslant R_0)$$
$$E_y = \frac{\lambda y}{2\pi\epsilon_0 r^2} \qquad (r \geqslant R_0).$$

Deriving an expression for the image plane coordinates (x_i, y_i) requires knowledge of how the deflection angles (α_x, α_y) change with proton position and electromagnetic field strength. As before, Δz denotes the proton path length integrated over the field region:

$$\alpha_x \approx \frac{e}{2\,\epsilon_\mathrm{p}} \int_{\Delta_z} E_x dz$$

$$= \frac{e}{2\,\epsilon_\mathrm{p}} \int_{\Delta_z} \frac{\lambda x}{2\pi\epsilon_0 r^2} dz$$
$$= \frac{e}{2\,\epsilon_\mathrm{p}} \left[\frac{\lambda x z}{2\pi\epsilon_0 r^2} \right]_{\Delta_z}$$
$$= \frac{e\lambda x \Delta z}{4\,\pi\epsilon_0\,\epsilon_\mathrm{p} r^2}$$

And similarly for y:

$$\alpha_y \approx \frac{e\lambda y \Delta z}{4\,\pi\epsilon_0\,\epsilon_\mathrm{p} r^2}. \tag{4}$$

The deflection equations can be simplified by defining $\mu_\mathrm{E} = \frac{e\lambda}{4\,\pi\epsilon_0\,\epsilon_\mathrm{p}}$:

$$\alpha_x = \frac{\mu_\mathrm{E} x \Delta z}{r^2}$$
$$\alpha_y = \frac{\mu_\mathrm{E} y \Delta z}{r^2}.$$

Now r_i can be extracted from x_i. Substituting the electric field equation for α_x into the definition of x_i:

$$x_i = Mx + D\alpha_x$$
$$= Mx + D\left[\frac{\mu_\mathrm{E} x \Delta z}{r^2}\right].$$

The same technique can applied to the y_i coordinate. Using $\mu_\mathrm{B} = \frac{e\mu_0 I}{2\pi\sqrt{2m_\mathrm{p}\epsilon_\mathrm{p}}}$ from [19], these equations can be expanded to account for the electric and magnetic fields:

$$x_i = Mx + \frac{Dx\Delta z}{r^2}(\mu_\mathrm{E} + \mu_\mathrm{B}) \tag{5}$$

$$y_i = My + \frac{Dy\Delta z}{r^2}(\mu_\mathrm{E} + \mu_\mathrm{B}). \tag{6}$$

Observing that $x_i = r_i\cos(\theta)$, equation (5) becomes:

$$r_i\cos(\theta) = Mr\cos(\theta) + \frac{D[r\cos(\theta)]\Delta z}{r^2}(\mu_\mathrm{E} + \mu_\mathrm{B}).$$

So the radial mapping for an infinite straight wire carrying a current I and charge per unit length λ reads:

$$r_i = Mr + \frac{D\Delta z}{r}(\mu_\mathrm{E} + \mu_\mathrm{B}). \tag{7}$$

Caustics arise when $\frac{dr_i}{dr} = 0$:

$$M - \frac{D\Delta z}{r^2}(\mu_\mathrm{E} + \mu_\mathrm{B}) = 0 \tag{8}$$

which yields

$$r^* = \sqrt{\frac{D\Delta z(\mu_\mathrm{E} + \mu_\mathrm{B})}{M}}. \tag{9}$$

The proton void radius is then the value of r_i when $r = r^*$:

$$r_i(r^*) = M\sqrt{\frac{D\Delta z(\mu_\mathrm{E} + \mu_\mathrm{B})}{M}} + \frac{D\Delta z}{\sqrt{\frac{D\Delta z(\mu_\mathrm{E}+\mu_\mathrm{B})}{M}}}(\mu_\mathrm{E} + \mu_\mathrm{B})$$
$$= \sqrt{MD\Delta z(\mu_\mathrm{E} + \mu_\mathrm{B})} + \sqrt{MD\Delta z(\mu_\mathrm{E} + \mu_\mathrm{B})}.$$

So the void radius in the image plane can be expressed in terms of the electromagnetic field geometry and magnitude, the system magnification and the proton energy:

$$r_\mathrm{v} = 2\sqrt{MD\Delta z(\mu_\mathrm{E} + \mu_\mathrm{B})}. \tag{10}$$

Equation (10) implies that $r_\mathrm{v} \propto I^{\frac{1}{2}}$ and $r_\mathrm{v} \propto \epsilon_p^{-\frac{1}{4}}$ for a proton beam passing through the magnetic field at the top a wire loop, whilst $r_\mathrm{v} \propto \lambda^{\frac{1}{2}}$ and $r_\mathrm{v} \propto \epsilon_\mathrm{p}^{-\frac{1}{2}}$ in the electric field around a charged wire. This is reasonable since proton deflection scales with the velocity v based on the Lorentz force and the amount of time the proton spends in the field. The electric field term scales as $1/v^2$ while the magnetic field term scales as $1/v$. For both an electric and magnetic field, the void radius is no longer a power law in ϵ_p, so electric field effects will cause a deviation from the $r_\mathrm{v} \propto \epsilon_\mathrm{p}^{-\frac{1}{4}}$ law.

ORCID iDs

P Bradford https://orcid.org/0000-0002-9618-6342
V T Tikhonchuk https://orcid.org/0000-0001-7532-5879
N C Woolsey https://orcid.org/0000-0002-2444-9027

References

[1] Consoli F *et al* 2020 Laser produced electromagnetic pulses: generation detection and mitigation *High Power Laser Sci. Eng.* **8** e22
[2] Kar S *et al* 2016 Guided post-acceleration of laser-driven ions by a miniature modular structure *Nat. Commun.* **7** 1–7
[3] Ahmed H, Kar S, Giesecke A L, Doria D, Nersisyan G, Willi O, Lewis C L S and Borghesi M 2017 Proton probing of laser-driven EM pulses travelling in helical coils *High Power Laser Sci. Eng.* **5** 1–5
[4] Bardon M *et al* 2020 Mitigation of strong electromagnetic pulses on the LMJ-PETAL facility *Phys. Rev. Res.* **2** 033502
[5] Sinenian N, Manuel M J-E, Frenje J A, Séguin F H, Li C K and Petrasso R D 2 2013 An empirical target discharging model relevant to hot-electron preheat in direct-drive implosions on OMEGA *Plasma Phys. Control. Fusion* **55** 045001
[6] Manuel M J-E *et al* 2012 Mapping return currents in laser-generated z-pinch plasmas using proton deflectometry *Appl. Phys. Lett.* **100** 203505

[7] Hicks D G *et al* 2000 Charged-particle acceleration and energy loss in laser-produced plasmas *Phys. Plasmas* **7** 5106–17

[8] Hohenberger M, Chang P-Y, Fiksel G, Knauer J P, Betti R, Marshall F J, Meyerhofer D D, Séguin F H and Petrasso R D 2012 Inertial confinement fusion implosions with imposed magnetic field compression using the omega laser *Phys. Plasmas* **19** 056306

[9] Goyon C *et al* 2017 Ultrafast probing of magnetic field growth inside a laser-driven solenoid *Phys. Rev.* E **95** 033208

[10] Moody J D *et al* 2020 Transient magnetic field diffusion considerations relevant to magnetically assisted indirect drive inertial confinement fusion *Phys. Plasmas* **27** 112711

[11] Bailly-Grandvaux M *et al* 2018 Guiding of relativistic electron beams in dense matter by laser-driven magnetostatic fields *Nat. Commun.* **9** 102

[12] Santos J J *et al* 2018 Laser-driven strong magnetostatic fields with applications to charged beam transport and magnetized high energy-density physics *Phys. Plasmas* **25** 056705

[13] Chien A *et al* 2019 Study of a magnetically driven reconnection platform using ultrafast proton radiography *Phys. Plasmas* **26** 062113

[14] Woolsey N C *et al* 2001 Collisionless shock and supernova remnant simulations on VULCAN *Phys. Plasmas* **8** 2439–45

[15] Pei X X *et al* 2016 Magnetic reconnection driven by Gekko XII lasers with a Helmholtz capacitor-coil target *Phys. Plasmas* **23** 032125

[16] Fiksel G, Fox W, Bhattacharjee A, Barnak D H, Chang P-Y, Germaschewski K, Hu S X and Nilson P M 2014 Magnetic reconnection between colliding magnetized laser-produced plasma plumes *Phys. Rev. Lett.* **113** 105003

[17] Bradford P *et al* 2020 Heathcote. Proton deflectometry of a capacitor coil target along two axes *High Power Laser Sci. Eng.* **8** e11

[18] Santos J J *et al* 2015 Laser-driven platform for generation and characterization of strong quasi-static magnetic fields *New J. Phys.* **17** 083051

[19] Gao L, Hantao J, Fiksel G, Fox W, Evans M and Alfonso N 2016 Ultrafast proton radiography of the magnetic fields generated by a laser-driven coil current *Phys. Plasmas* **23** 043106

[20] Peebles J L, Davies J R, Barnak D H, Cracium T, Bonino M J and Betti R 2020 Axial proton probing of magnetic and electric fields inside laser-driven coils *Phys. Plasmas* **27** 063109

[21] Tikhonchuk V T, Bailly-Grandvaux M, Santos J J and Poyé A 2017 Quasistationary magnetic field generation with a laser-driven capacitor-coil assembly *Phys. Rev.* E **96** 023202

[22] Fiksel G, Fox W, Gao L and Hantao J 2016 A simple model for estimating a magnetic field in laser-driven coils *Appl. Phys. Lett.* **109** 134103

[23] Courtois C, Ash A D, Chambers D M, Grundy R A D and Woolsey N C 2005 Creation of a uniform high magnetic-field strength environment for laser-driven experiments *J. Appl. Phys.* **98** 054913

[24] Wang W *et al* 2018 Efficient production of strong magnetic fields from ultraintense ultrashort laser pulse with capacitor-coil target *Phys. Plasmas* **25** 083111

[25] Ivanov V V *et al* 2020 Study of laser-driven magnetic fields with a continuous wave Faraday rotation diagnostic *Phys. Plasmas* **27** 033102

[26] Morita H, Pollock B B, Goyon C S, Williams G J, Farley Law K F, Fujioka S and Moody J D 2021 Dynamics of laser-generated magnetic fields using long laser pulses *Phys. Rev.* E **103** 033201

[27] Daido H, Mima K, Miki F, Fujita M, Kitagawa Y, Nakai S and Yamanaka C 1987 Ultrahigh pulsed magnetic field produced by a CO_2 laser *Japan. J. Appl. Phys.* **26** 1290–5

[28] McKenna P, Lindau F, Lundh O, Neely D, Persson A and Claes-Göran W 2006 High-intensity laser-driven proton acceleration: influence of pulse contrast *Phil. Trans. R. Soc.* A **364** 711–23

[29] Kumar D *et al* 2020 Magnetic field generation using single-plate targets driven by kJ-ns class laser *Plasma Phys. Control. Fusion* **62** 125024

[30] Zhu B J *et al* 2015 Strong magnetic fields generated with a simple open-ended coil irradiated by high power laser pulses *Appl. Phys. Lett.* **107** 261903

[31] Danson C and Paul M 2021 HPLSE editorial tribute to professor David Neely *High Power Laser Sci. Eng.* **9** e7

[32] Danson C N *et al* 2019 Petawatt and exawatt class lasers worldwide *High Power Laser Sci. Eng.* **7** e54

[33] Jarrett J *et al* 2019 Reflection of intense laser light from microstructured targets as a potential diagnostic of laser focus and plasma temperature *High Power Laser Sci. Eng.* **7** e2

[34] Scott G G *et al* 2017 Diagnosis of Weibel instability evolution in the rear surface density scale lengths of laser solid interactions via proton acceleration *New J. Phys.* **19** 043010

[35] Bellei C *et al* 2010 Micron-scale fast electron filaments and recirculation determined from rear-side optical emission in high-intensity laser–solid interactions *New J. Phys.* **12** 073016

[36] Liao G *et al* 2019 Multimillijoule coherent terahertz bursts from picosecond laser-irradiated metal foils *Proc. Natl Acad. Sci.* **116** 3994–9

[37] Bradford P *et al* 2018 EMP control and characterization on high-power laser systems *High Power Laser Sci. Eng.* **6** e21

[38] Scott G G *et al* 2015 Optimization of plasma mirror reflectivity and optical quality using double laser pulses *New J. Phys.* **17** 033027

[39] Nürnberg F *et al* 2009 Radiochromic film imaging spectroscopy of laser-accelerated proton beams *Rev. Sci. Instrum.* **80** 033301

[40] Cecchetti C A *et al* 2009 Magnetic field measurements in laser-produced plasmas via proton deflectometry *Phys. Plasmas* **16** 043102

[41] Romagnani L *et al* 2008 Proton probing measurement of electric and magnetic fields generated by ns and ps laser-matter interactions *Laser Part. Beams* **26** 241–8

[42] Quinn K *et al* 2009 Laser-driven ultrafast field propagation on solid surfaces *Phys. Rev. Lett.* **102** 194801

[43] Liu H *et al* 2018 Cherenkov radiation-based optical fibre diagnostics of fast electrons generated in intense laser-plasma interactions *Rev. Sci. Instrum.* **89** 083302

[44] Liu H *et al* 2019 Study of backward terahertz radiation from intense picosecond laser–solid interactions using a multichannel calorimeter system *High Power Laser Sci. Eng.* **7** e6

[45] Carroll D C, Brummitt P, Neely D, Lindau F, Lundh O, Wahlström C-G and McKenna P 2010 A modified Thomson parabola spectrometer for high resolution multi-MeV ion measurements–application to laser-driven ion acceleration *Nucl. Instrum. Methods Phys. Res.* A **620** 23–7

[46] Neely D, Foster P, Robinson A, Lindau F, Lundh O, Persson A, Wahlström C-G and McKenna P 2006 Enhanced proton beams from ultrathin targets driven by high contrast laser pulses *Appl. Phys. Lett.* **89** 021502

[47] Tresca O *et al* 2011 Controlling the properties of ultraintense laser–proton sources using transverse refluxing of hot electrons in shaped mass-limited targets *Plasma Phys. Control. Fusion* **53** 105008

[48] Gonzalez-Izquierdo B *et al* 2016 Towards optical polarization control of laser-driven proton acceleration in foils

undergoing relativistic transparency *Nat. Commun.* **7** 1–10
[49] Simpson R A *et al* 2021 Scaling of laser-driven electron and proton acceleration as a function of laser pulse duration, energy and intensity in the multi-picosecond regime *Phys. Plasmas* **28** 013108
[50] Rusby D R, Armstrong C D, Scott G G, King M, McKenna P and Neely D 2019 Effect of rear surface fields on hot, refluxing and escaping electron populations via numerical simulations *High Power Laser Sci. Eng.* **7** e45
[51] Consoli F *et al* 2021 Sources and space-time distribution of the electromagnetic pulses in experiments on inertial confinement fusion and laser-plasma acceleration *Phil. Trans. R. Soc.* A **379** 20200022
[52] Armstrong C D *et al* 2019 Bremsstrahlung emission from high power laser interactions with constrained targets for industrial radiography *High Power Laser Sci. Eng.* **7** e24
[53] Liao G-Q *et al* 2020 Towards terawatt-scale spectrally tunable terahertz pulses via relativistic laser-foil interactions *Phys. Rev.* X **10** 031062
[54] Bradford P 2020 Data Repository Dual-axis proton deflectometry of a capacitor coil target (https://doi.org/10.15124/79ca0a38-dddb-480c-9edf-d8f52496dfad)
[55] Cikhardt J *et al* 2014 Measurement of the target current by inductive probe during laser interaction on terawatt laser system pals *Rev. Sci. Instrum.* **85** 103507
[56] Dubois J L *et al* 2014 Target charging in short-pulse-laser-plasma experiments *Phys. Rev.* E **89** 1–15
[57] Pearlman J S and Dahlbacka G H 1977 Charge separation and target voltages in laser-produced plasmas *Appl. Phys. Lett.* **31** 414–17
[58] Consoli F, De Angelis R, Duvillaret L, Andreoli P L, Cipriani M, Cristofari G, Di Giorgio G, Ingenito F and Verona C 2016 Time-resolved absolute measurements by electro-optic effect of giant electromagnetic pulses due to laser-plasma interaction in nanosecond regime *Sci. Rep.* **6** 27889
[59] Poyé A *et al* 2015 Dynamic model of target charging by short laser pulse interactions *Phys. Rev.* E **92** 043107
[60] Benjamin R F, McCall G H and Ehler A W 1979 Measurement of return current in a laser-produced plasma *Phys. Rev. Lett.* **42** 890–3
[61] Williams G J *et al* 2020 Laser intensity scaling of the magnetic field from a laser-driven coil target *J. Appl. Phys.* **127** 083302
[62] Krása J *et al* 2017 Spectral and temporal characteristics of target current and electromagnetic pulse induced by nanosecond laser ablation *Plasma Phys. Control. Fusion* **59** 065007
[63] Damien F G Minenna A P, Bradford P, Woolsey N and Tikhonchuk V T 2020 Electromagnetic pulse emission from target holders during short-pulse laser interactions *Phys. Plasmas* **27** 063102
[64] Kugland N L, Ryutov D D, Plechaty C, Ross J S and Park H S 2012 Invited Article: relation between electric and magnetic field structures and their proton-beam images *Rev. Sci. Instrum.* **83** 101301